Acta Pharmaceutica Sinica B 2024;14(2):751−764

Chinese Pharmaceutical Association
Institute of Materia Medica, Chinese Academy of Medical Sciences

Acta Pharmaceutica Sinica B

www.elsevier.com/locate/apsb
www.sciencedirect.com

ORIGINAL ARTICLE

Tumor-targeted metabolic inhibitor prodrug labelled with cyanine dyes enhances immunoprevention of lung cancer

Wen Li[a,b,†], Jiali Huang[a,b,†], Chen Shen[a,c,†], Weiye Jiang[a,c], Xi Yang[a,b], Jingxuan Huang[a,c], Yueqing Gu[a,b], Zhiyu Li[a,c,*], Yi Ma[a,b,*], Jinlei Bian[a,c,*]

[a]*State Key Laboratory of Natural Medicines, China Pharmaceutical University, Nanjing 210009, China*
[b]*Department of Biomedical Engineering, School of Engineering, China Pharmaceutical University, Nanjing 210009, China*
[c]*Jiangsu Key Laboratory of Drug Design and Optimization, Department of Medicinal Chemistry, School of Pharmacy, China Pharmaceutical University, Nanjing 210009, China*

Received 29 June 2023; received in revised form 28 September 2023; accepted 17 October 2023

KEY WORDS

Smart prodrug system;
Glutamine antagonists;
Immunotherapy;
Photodynamic therapy;
Reactive oxygen species;
Metabolic inhibitor;
Cyanine dye;
Non-small-cell lung cancer (NSCLC)

Abstract Recent progress in targeted metabolic therapy of cancer has been limited by the considerable toxicity associated with such drugs. To address this challenge, we developed a smart theranostic prodrug system that combines a fluorophore and an anticancer drug, specifically 6-diazo-5-oxo-L-norleucine (DON), using a thioketal linkage (TK). This system enables imaging, chemotherapy, photodynamic therapy, and on-demand drug release upon radiation exposure. The optimized prodrug, DON-TK-BM3, incorporating cyanine dyes as the fluorophore, displayed potent reactive oxygen species release and efficient tumor cell killing. Unlike the parent drug DON, DON-TK-BM3 exhibited no toxicity toward normal cells. Moreover, DON-TK-BM3 demonstrated high tumor accumulation and reduced side effects, including gastrointestinal toxicity, in mice. This study provides a practical strategy for designing prodrugs of metabolic inhibitors with significant toxicity stemming from their lack of tissue selectivity.

*Corresponding authors.
E-mail addresses: zhiyuli@cpu.edu.cn (Zhiyu Li), yima.ant@163.com (Yi Ma), bianjl@cpu.edu.cn (Jinlei Bian).
[†]These authors made equal contributions to this work.

Peer review under the responsibility of Chinese Pharmaceutical Association and Institute of Materia Medica, Chinese Academy of Medical Sciences.

https://doi.org/10.1016/j.apsb.2023.10.020

1. Introduction

Targeting cancer metabolism therapeutically has experienced a research upsurge since the Warburg effect was hypothesized one hundred years ago[1,2]. More recently, reprogrammed energy metabolism has been widely accepted for its ability to enhance the substrate generation needed for tumor cell biomass[3−5]. However, strategic advances in targeted cancer metabolic therapy have faced challenges, with only a few metabolism-based drugs, including inhibitors targeting isocitrate dehydrogenase, receiving approval from the US Food and Drug Administration (FDA) as anticancer therapies[6,7]. The limited approvals can be attributed to the significant toxicity of most metabolism-based drugs on normal cells and tissues, which narrows their therapeutic index. For example, 6-diazo-5-oxo-L-norleucine (DON) was developed to target glutamine metabolism. However, it was discontinued in clinical studies due to severe gastrointestinal toxicity[8−12]. Although the prodrug strategy could mitigate the side effects of metabolic drugs on normal tissues, the existence of off-target effects poses a hidden danger to disease treatment and can affect the prognosis[13,14]. Hence, the development of smart therapeutics with stimulus-release drugs and indicative functions is needed to enhance the bioavailability and reduce the side effects of tumor-targeted metabolic inhibitors.

Photocages are light-sensitive groups that utilize the spatial and temporal resolution of light as a stimulus to restore the activity of parent drugs reducing systemic toxicity[15]. Extending their use towards therapeutic purposes requires shifting their absorption to the near-infrared (NIR) phototherapeutic window (650−900 nm), within the relevant wavelength range for the body[16]. However, the development of such methods faces significant chemical challenges[17]. Uncaging reactions initiated by an easily attainable single-photon flux of NIR light are relatively rare compared to those relying on UV or blue light. The low energy of NIR photons hinders the direct achievement of efficient bond cleavage in living tissues[18]. Therefore, rationally developing an external stimuli-responsive smart strategy is crucial for designing NIR light-based metabolic inhibitor prodrugs.

Benefiting from their useful near-IR fluorescent properties and excellent biological compatibility, heptamethine cyanines have been extensively utilized in preclinical and clinical imaging[19]. These cyanine dyes offer several advantages, including maximum absorbances in the NIR window (650−900 nm), low background absorbance interference, and low toxicity.

Herein, we present an indocyanine-based strategy for the treatment of lung cancer using NIR light-activated prodrugs (Fig. 1). The indocyanine moiety not only serves as a photocage, but also contributes to the phototherapy. When activated by NIR light, the cyanine dyes can simultaneously generate both reactive oxygen species (ROS) and local heat. Currently, there is limited research on the development of an NIR-triggered ROS-sensitive prodrug for metabolic phototherapy.

In this study, we present a versatile and novel strategy for constructing a metabolic inhibitor (DON)-based prodrug using thioketal (TK) as a ROS-responsive linker[20]. Our aim is to enable *in vivo* imaging-guided metabolic phototherapy with on-demand drug release triggered by a single NIR light irradiation. Three prodrugs (DON-TK-BM1, DON-TK-BM2, and DON-TK-BM3, Fig. 2A) with different cyanine-based photocages were designed and synthesized. Among them, DON-TK-BM3, optimized by adjusting the hydrophilicity and Stokes shift, demonstrated the best performance.

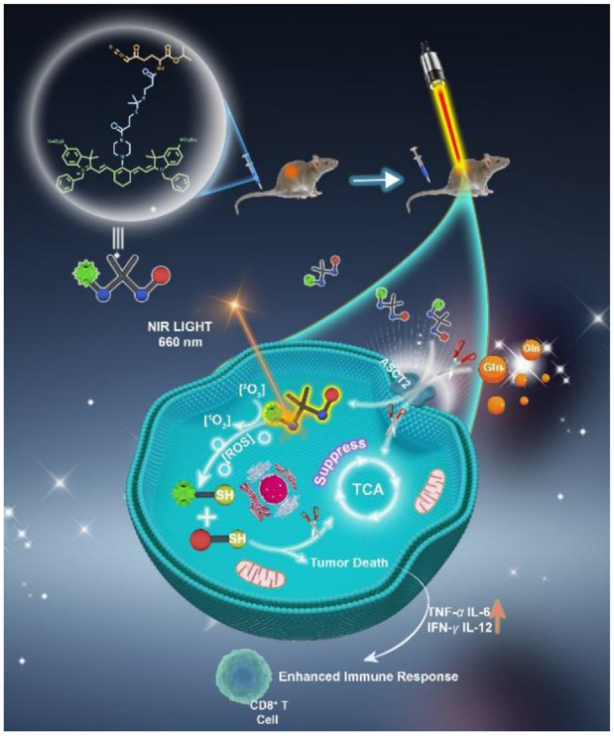

Figure 1 Schematic illustration of drug release and antitumor platform of glutamine antagonist DON prodrug (DON-TK-BM3).

Utilizing the high dependence of tumor cells on glutamine, DON (the target head of DON-TK-BM3) with a similar structure to glutamine can accumulate in tumor tissues, providing valuable "Where" information for the diagnosis of disease. Under 660 nm laser irradiation, the ROS produced by BM3 can break the TK linkage, enabling on-demand drug release and addressing the question "How". Furthermore, structural changes before and after the release of DON from DON-TK-BM3 alter the fluorescence spectrum, providing information about the timing ("When") of drug release. Ultimately, DON-TK-BM3 simultaneously provides a photodynamic therapy (PDT), inhibits the tricarboxylic acid cycle (TCA) of tumor cells, reverses the immunosuppressive microenvironment of the tumor, and achieves a potent anti-tumor effect (Fig. 1). This smart theranostic prodrug system represents a simple platform with multiple functions and provides a promising strategy for therapeutically targeting cancer metabolism.

2. Results and discussion

2.1. *Design of the smart prodrug system*

We coupled the meso-Cl of cyanine dyes with a ROS-responsive thioketal linker (TK) covalently. The other end of the linker was coupled to the amino group of DON in a similar manner. Upon ROS-induced cleavage, the disruption of intramolecular charge transfer resulted in different spectral characteristics between the uncoupled and coupled cyanine dyes. This lays the foundation for the monitoring mechanism of prodrug activation. The released drug DON inhibits tumor growth by blocking the TCA and reversing the suppressive tumor immune microenvironment. These theranostic prodrugs remain inactive in normal cells but are activated specifically at the tumor site, reducing off-target toxicity

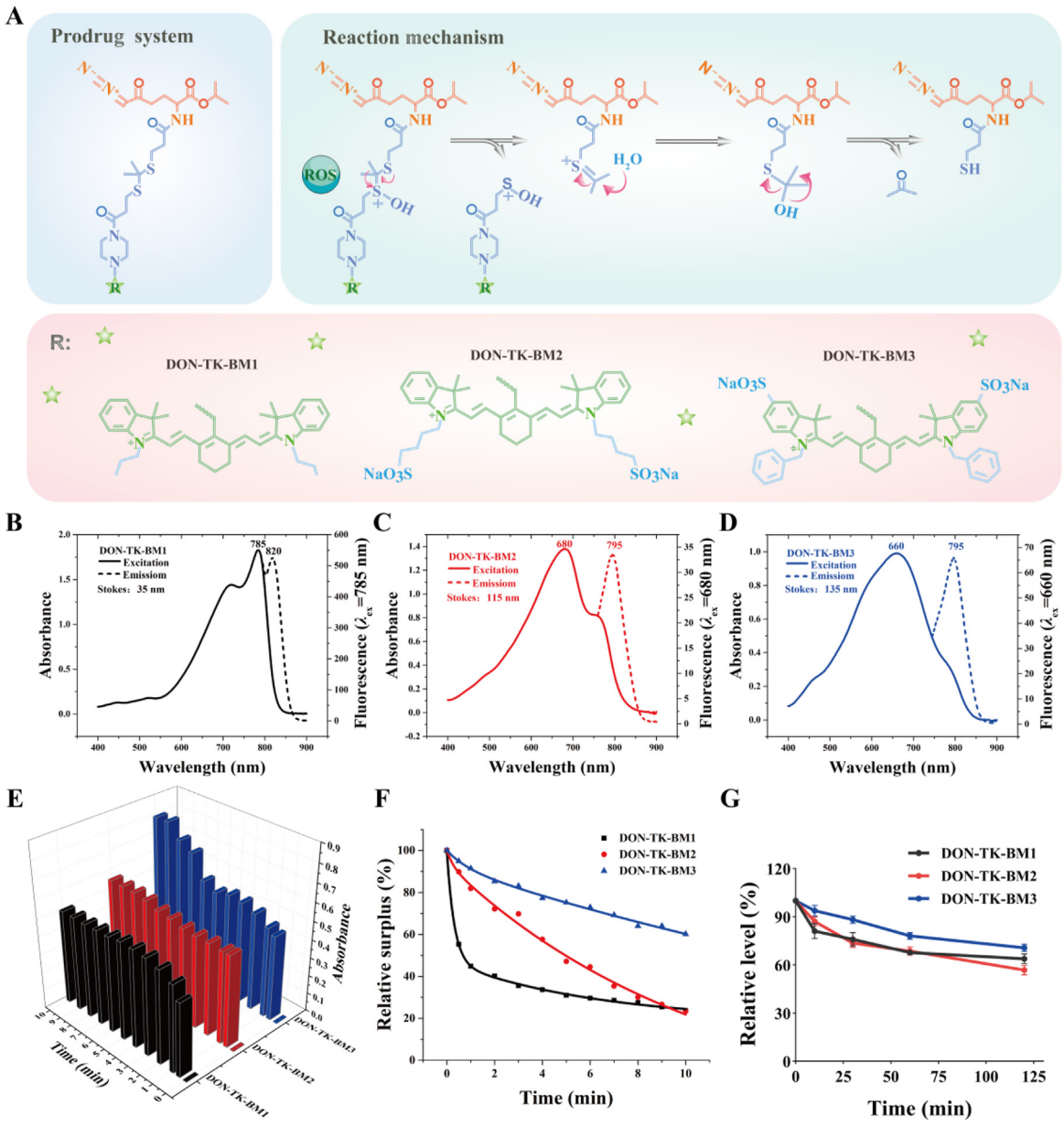

Figure 2 Screening of prodrugs. (A) Design and mechanism of the smart prodrug system; (B) UV absorption spectra; (C) fluorescence emission spectra; (D) and Stokes shift of prodrugs; (E) Prodrug-induced active oxygen species production; (F) Stability of prodrugs under laser irradiation for 10 min; (G) Plasma stability of DON-TK-BM1, DON-TK-BM2 and DON-TK-BM3.

and improving the therapeutic index of chemotherapy. We synthesized three candidate prodrugs (named DON-TK-BM1, DON-TK-BM2, and DON-TK-BM3, Fig. 2A) and characterized their molecular structures using nuclear magnetic resonance spectroscopy and high-resolution mass spectrometry (MS) (Supporting Information Schemes S24−S35).

2.2. *Chemistry*

The synthetic routes for DON-TK-BMs are shown in Scheme 1. Briefly, cyanine dyes (**5**, **6**, **7**), TK linker (**9**) and (*S*)-2-amino-6-diazo-5-oxohexanoic acid (**8**) were synthesized as described in Supporting Information Schemes S1 and S2. Amide **10** was obtained through condensation of **8** and **9**. It was further condensed with piperazine to yield **11**. The respective cyanine dyes were reacted with intermediate **11** to obtain **12**−**14**. The TK linker was replaced with sebacic acid, and the subsequent reaction conditions are presented in Supporting Information Scheme S3. Similarly, L-phenylalanine was esterified with isopropyl to obtain **18**, which was condensed with the TK linker to yield **19** (Scheme S3). The subsequent reaction steps were similar to those for compound **14**.

2.3. *Screening of the smart prodrug system*

To identify smart theranostic prodrugs with favorable physical and chemical properties, DON-TK-BMs was investigated in terms of solubility, spectral properties, photostability, plasma stability and targeting. As shown in Supporting Information Fig. S1, DON-TK-

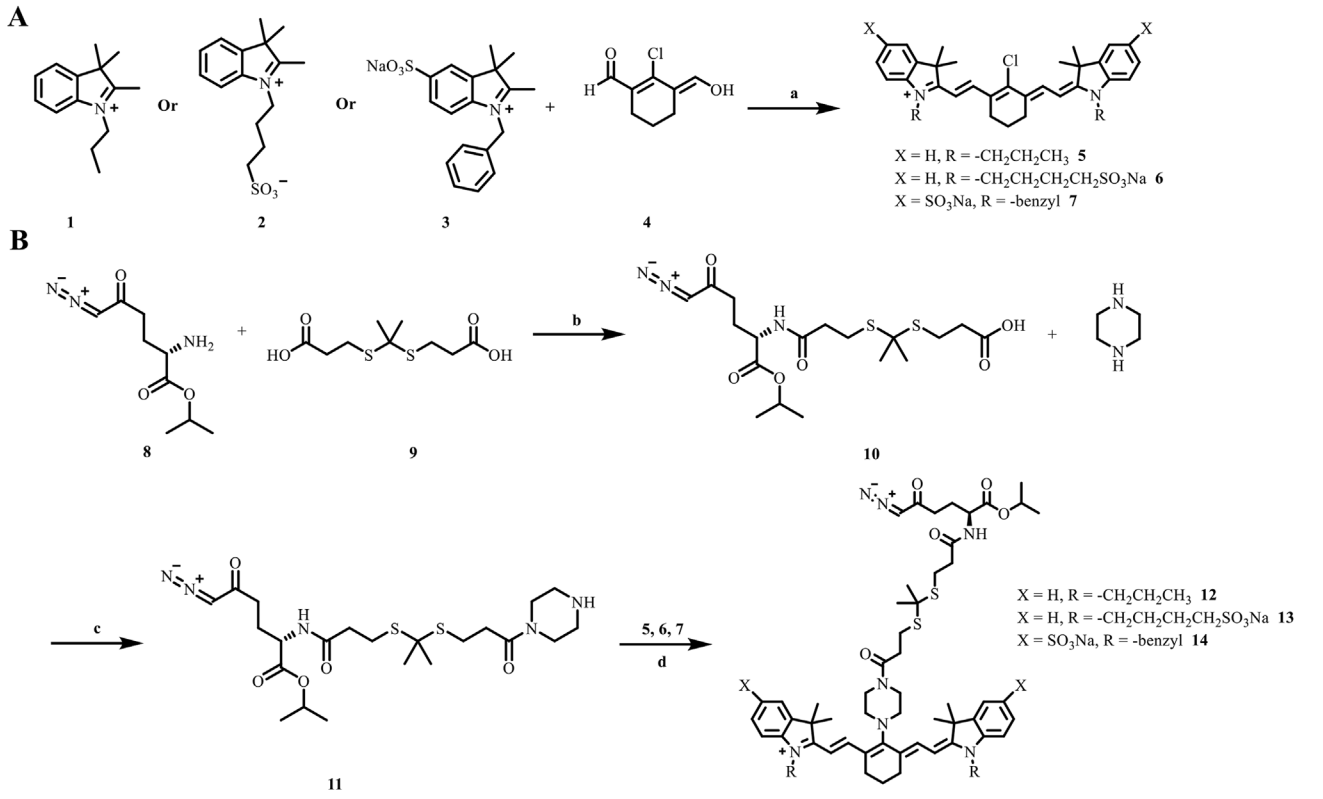

Scheme 1 Synthesis of the BMs (compounds **5**−**7**) and DON-TK-BMs (compounds **12**−**14**). (A) Synthesis of the BMs. Reagents and conditions: (a) CH_3COONa, $(CH_3CO)_2O$, 4 h, 83%. (B) Synthesis of DON-TK-BMs. Reagents and conditions: (b) HATU, DIPEA, DCM, rt, 2 h, 47%; (c) HATU, DIPEA, DCM, rt, 2 h, 25%; (d) compounds **5**−**7**, DMF, rt, dark, 10%.

BM1 formed aggregates in an aqueous solution, whereas DON-TK-BM2 and DON-TK-BM3 exhibited good water solubility due to the presence of sulfonic acid groups, which imparted strong hydrophilicity. The maximum absorption and emission peaks of the prodrugs were measured using an ultraviolet spectrophotometer and fluorescence spectrophotometer, respectively (Fig. 2B–D). Among them, DON-TK-BM3 had the largest Stokes shift, with a maximum absorption peak at 658 nm. Under excitation with 660 nm light, it exhibited quite strong fluorescence at 795 nm, indicating its potential as a detection reagent.

Next, the reactive oxygen production efficiency of the prodrugs under light was measured. As shown in Fig. 2E, DON-TK-BM3 produced the highest amount of ROS within 10 min, while DON-TK-BM1 and DON-TK-BM2 reached saturation at approximately 6 min. This indicates that DON-TK-BM3 had better drug release potential. We then compared the photostability of the prodrugs by evaluating the absorbance values after laser irradiation for 10 min. The absorbance value of DON-TK-BM1 and DON-TK-BM2 dramatically decreased, while DON-TK-BM3 retained more than 60% of its absorbance after 10 min (Fig. 2F). What's more, DON-TK-BM3 also maintained good integrity in plasma as shown in Fig. 2G. Meanwhile, the retention of DON-TK-BM2 and DON-TK-BM3 in Lewis lung cancer (LLC) was assessed (Supporting Information Fig. S2). The luminescence efficiency of DON-TK-BM3 in the subcutaneous tumor was higher than that of DON-TK-BM2. Furthermore, the fluorescence signal was still noticeable after 10 h. These results demonstrate that DON-TK-BM3 possesses better photostability and tumor-targeting abilities, which can extend the indication time and improve the treatment efficiency.

Overall, these results indicate that DON-TK-BM3 aligns better with the requirements of a smart theranostic prodrug and can be used for further applications. For further studies, the non-cleaved DON-CC-BM3 (in which the TK linker was replaced by a ROS-insensitive alkyl linker) was synthesized as a negative control using the same reaction steps and conditions (Supporting Information Fig. S3).

2.4. *In vitro ROS generation and drug release*

ROS is the prerequisite factor for the rupture of the thioketal bond. Therefore, to verify the feasibility of prodrug-responsive release, the generation of ROS was determined using the UV absorption change of the ROS-sensitive probe, 2′-7′-dichlorodihydrofluorescein (preprocessed as 2′-7′-dichlorodihydrofluorescein diacetate probe). As shown in Fig. 3B, with the increase of irradiation time, the UV absorption of DCF at 530 nm became stronger, indicating an increase in ROS production by DON-TK-BM3. The ROS signal produced by DON-TK-BM3 was higher than that of DON-CC-BM3 (Supporting Information Fig. S4). The breakage of the TK linkage consumed ROS and ensured the structural stability of the photosensitive group BM3, allowing DON-TK-BM3 to produce more ROS (Fig. 3C). To evaluate the ROS generation capability under physiological conditions, fluorescence microscopy and flow cytometry were used (Supporting Information Fig. S5). The DON-TK-BM3 with laser irradiation group (DON-TK-BM3+hv) produced higher intracellular ROS than the DON-CC-BM3 with laser irradiation group (DON-CC-BM3+hv), while low detectable ROS were generated in BM3-or DON-treated blank cells.

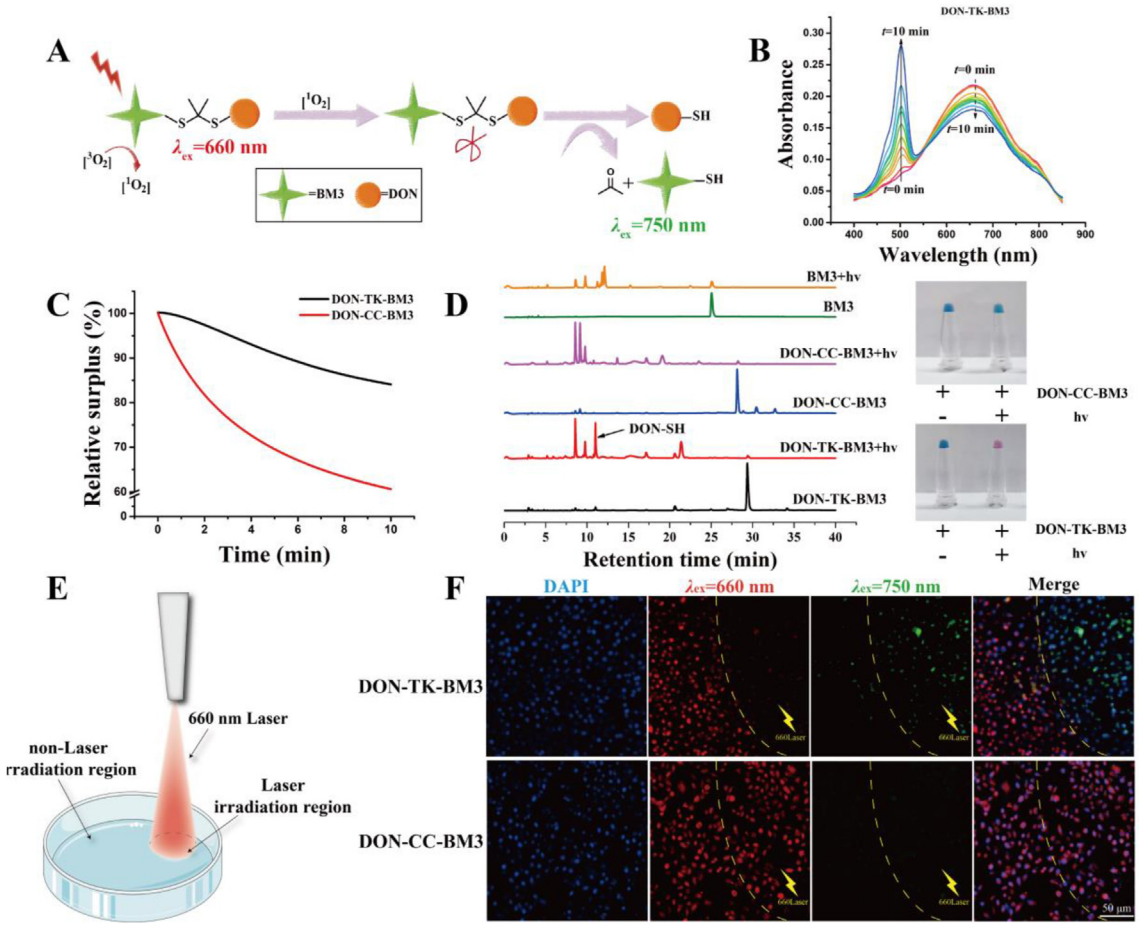

Figure 3 *In vitro* ROS generation and drug release under 660 nm laser irradiation. (A) Schematic diagram showing ROS mediated thioketal linker cleavage and cascaded DON release; (B) UV absorption spectrum showing increased ROS production with laser irradiation time; (C) Stability of different samples under laser irradiation at various time points; (D) HPLC chromatograms of DON-TK-BM3, DON-CC-BM3, and BM3 measured at 254 nm under different treatment; (E) Schematic diagram showing drug release process of DON-TK-BM3 under laser irradiation in A549 cells; (F) Fluorescence live cell images of A549 cells under different treatments. All drug concentrations were 2×10^{-6} mol/L; scale bar: 50 μm.

To evaluate the ROS-induced release of DON, we characterized the structural changes of DON-TK-BM3 under laser irradiation using high-performance liquid chromatography (HPLC). As shown in Fig. 3D, DON-TK-BM3 exhibited a peak at a retention time of 29.40 min. After 5 min of irradiation, the original peak completely degraded, and new peaks appeared at retention times of 7−12 min. We further analyzed the components generating the new peaks using HPLC−MS and confirmed that the peak at a retention time of 11.10 min corresponded to our targeted therapeutic agent DON-SH, with a mass-to-charge ratio (*m*/*z*) of 324.0976 (Supporting Information Fig. S6). The other peaks were possibly attributed to side products generated due to the very high reactivity of ROS. Despite the attachment of a short thiol ligand to DON after TK linker cleavage, previous studies[11,12] and our experimental results have demonstrated the potent efficacy of the DON derivative. Conversely, as a ROS-insensitive compound, DON-CC-BM3 did not produce any significant signal peak at 11.10 min under the same laser irradiation, indicating that the TK linkage was crucial for ROS-responsive drug release. Furthermore, to elucidate the release mechanism and detect the active component, LPH-TK-BM3 was synthesized by replacing DON with a simpler and more stable phenylalanine. As shown in Supporting Information Fig. S7, LPH-TK-BM3 exhibited a peak at a retention time of 16.554 min. After 5 min of irradiation, the original peak degraded, and a new peak at a retention time of 17.235 min appeared, which was consistent with that of the control LPH-SH. The mass spectrum data also confirmed that the new peak at a retention time of 17.235 min corresponded to the expected product LPH-SH. Accordingly, we determined that DON-TK-BM3 was similarly cleaved, releasing the active intermediate DON-SH. It may also be worth noting that through the comparison of cell efficacy tests, we proved that the presence of ROS did not affect the original efficacy of DON (Supporting Information Fig. S8).

We further investigated intracellular laser-induced drug release. To observe the effect of 660 nm laser irradiation on drug release, a confocal culture dish containing A549 cells was divided into a laser irradiation region and a non-laser irradiation region by controlling the irradiation range of the laser (Fig. 3E). By monitoring the fluorescence spectrum of DON-TK-BM3 before (λ_{Ex} = 660 nm) and after (λ_{Ex} = 750 nm) the fracture of TK linkage, the laser-triggered release of DON could be observed through changes in the fluorescence signal (Supporting

Information Fig. S9). As shown in Fig. 3F, the red signal (λ_{Ex} = 660 nm) of DON-TK-BM3 was significantly lower in the laser irradiation region than in the non-irradiation region. Furthermore, a green signal (λ_{Ex} = 750 nm) appeared in the laser-irradiation region. The distinct fluorescence difference between inside and outside the illumination boundary indicated the accurate release of DON from DON-TK-BM3 under laser irradiation, providing potential for reducing the impact on normal cells and tissues. No changes were observed in the DON-CC-BM3 group, as the CC linkage could not be cleaved by laser-trigged ROS.

2.5. *Cellular uptake and subcellular localization*

To investigate the cellular uptake mechanism of DON-TK-BM3, we examined its interaction with the ASCT2 protein, a cell membrane surface transporter responsible for glutamine uptake. First, we used MOE molecular docking software to determine the binding of DON-TK-BM3 to ASCT2. DON-TK-BM3 was able to bind to the same binding pocket of ASCT2 as DON, while the larger molecular volume of the probe caused some differences in the surrounding amino acid residues (Supporting Information Fig. S10). Residual Cys467 was revealed to form covalent bond with the diazo group of DON-TK-BM3. Meanwhile, Ser353, Ser354 and Asp464 could form hydrogen bonds with the probe. The total binding free energy of DON-TK-BM3 was −13.1913 kcal/mol, slightly higher than that of DON was −14.6519 kcal/mol. These results showed that DON-TK-BM3 could directly bind to ASCT2, despite that the binding strength was slightly weaker than that of DON. Then, the cellular pathway of DON-TK-BM3 was further studied by experiment. Non-small-cell lung cancer (NSCLC) cell lines (A549 and H1975) and a human bronchial epithelial cell line (16HBE) were selected for the *in vitro* experiments based on their different levels of expression of ASCT2, as confirmed by Western blot and polymerase chain reaction (Fig. 4A and B). For A549 cells highly expressing ASCT2, DON-TK-BM3 exhibited bright fluorescence in the cytoplasm, indicating its internalization (Fig. 4C). Conversely, the fluorescence signal of DON-TK-BM3 was only slightly observed in H1975 and 16HBE cells, which possess low ASCT2 expression. Flow cytometry results were consistent with the fluorescence imaging (Supporting Information Fig. S11). To further confirm the role of ASCT2 in DON-TK-BM3 uptake, siRNA transfection was used to artificially reduce the expression of ASCT2 protein in A549 cells (Supporting Information Fig. S12), then flow cytometry and confocal microscopy imaging were used to compare the differences in DON-TK-BM3 uptake by ASCT2 KO A549 cells and normal A549 cells. As shown in Fig. 4D and E, after reducing the expression of ASCT2 protein in A549 cells, the uptake of DON-TK-BM3 in ASCT2 KO A549 cells was significantly lower than that in normal A549 cells. Further, we used V-9302, a competitive inhibitor of ASCT2. Preincubation with V-9302 significantly reduced the intracellular fluorescence signal of DON-TK-BM3 (Supporting Information Fig. S13), the above experiments confirmed the specific ASCT2-mediated internalization in A549 cells. Additionally, the intracellular fate of DON-TK-BM3 was determined. The localization of DON-TK-BM3 with mitochondria, lysosomes, and Golgi apparatus was determined by confocal microscopy, and Pearson coefficient was used as reference. Our data revealed that DON-TK-BM3 strongly colocalized with mitochondria, with a Pearson's coefficient of 0.789 (Fig. 4F, Supporting Information Fig. S14). These suggested that DON-TK-BM3 may exert its effects on cells by influencing mitochondrial functions.

2.6. *Cell damage and metabolic inhibition*

The antitumor efficacy of DON-TK-BM3 was evaluated *in vitro* using A549, H1975, and 16HBE cells. As shown in Fig. 5A, DON-TK-BM3 had a similar inhibitory effect on A549 cells as free DON. However, this inhibitory effect was significantly reduced in H1975 and 16HBE cells, probably due to the limited expression of ASCT2 which impeded the cellular uptake of DON-TK-BM3. The control substance, DON-CC-BM3 did not show cytotoxicity independent of the presence of irradiation. *In vitro* studies further confirmed that laser irradiation significantly increased the cytotoxicity of DON-TK-BM3, with an IC_{50} of 1.5×10^{-6} mol/L in A549 cells (Supporting Information Fig. S15).

Considering that DON-TK-BM3 therapy altered the cellular microenvironment by blocking redox and glutamine metabolism, we investigated changes in cellular energy and amino acid metabolism following different treatments. Our results demonstrated that ATP production, basal oxygen consumption rate (OCR), and maximal OCR were substantially reduced after treatment with DON-TK-BM3 compared to control, indicating its efficient ability to reduce the intracellular energy supply in cancer cells (Fig. 5B and C).

The impact of glutamine metabolism suppression on the levels of intracellular metabolites was evaluated in A549 cancer cells. Besides the expected effects on glutamine and glutamate, DON-TK-BM3+hv significantly reduced the content of α-ketoglutarate in the TCA cycle and decreased the levels of glutathione, indicating its ability to suppress energy production in A549 cells (Fig. 5D).

To further explore the impact of DON-TK-BM3 on signaling pathways associated with glutamine metabolism, A549 cancer cells were treated with the compound under hv. As shown in Fig. 5E, DON-TK-BM3 + hv treatment inhibited the cancer cell proliferation marker C-myc and upregulated the expression of the apoptosis marker caspase 3. This suggests that the combined treatment of DON and PDT effectively suppressed tumor proliferation and promoted tumor cell apoptosis. The phosphorylation of extracellular signal-regulated kinase (ERK) and protein kinase B (AKT) was also reduced in A549 cells, indicating that DON-TK-BM3 + hv prevented the activation of the AKT/mammalian target of rapamycin pathway. Collectively, DON-TK-BM3 + hv induced changes in the tumor microenvironment characterized by alterations in redox and amino acid metabolism, ultimately leading to the apoptosis of tumor cells.

2.7. *Biodistribution and antitumor efficacy of DON-TK-BM3 in A549 cell tumor model*

In vivo biodistribution studies were conducted to examine the distribution pattern of DON-TK-BM3 in subcutaneous tumors using A549 and H1975 xenograft mouse models (Fig. 6A). Consistent with the cell uptake selectivity data, the high fluorescence intensity of DON-TK-BM3 was observed in A549 tumors, peaking at 1 h and remaining detectable for up to 24 h. BM3 alone was used as the control. Its fluorescence signal in A549 tumors was weak, indicating that the high targeting ability of DON-TK-BM3 resulted from the targeting group DON, which has a similar structure to glutamine. Additional time points of DON-

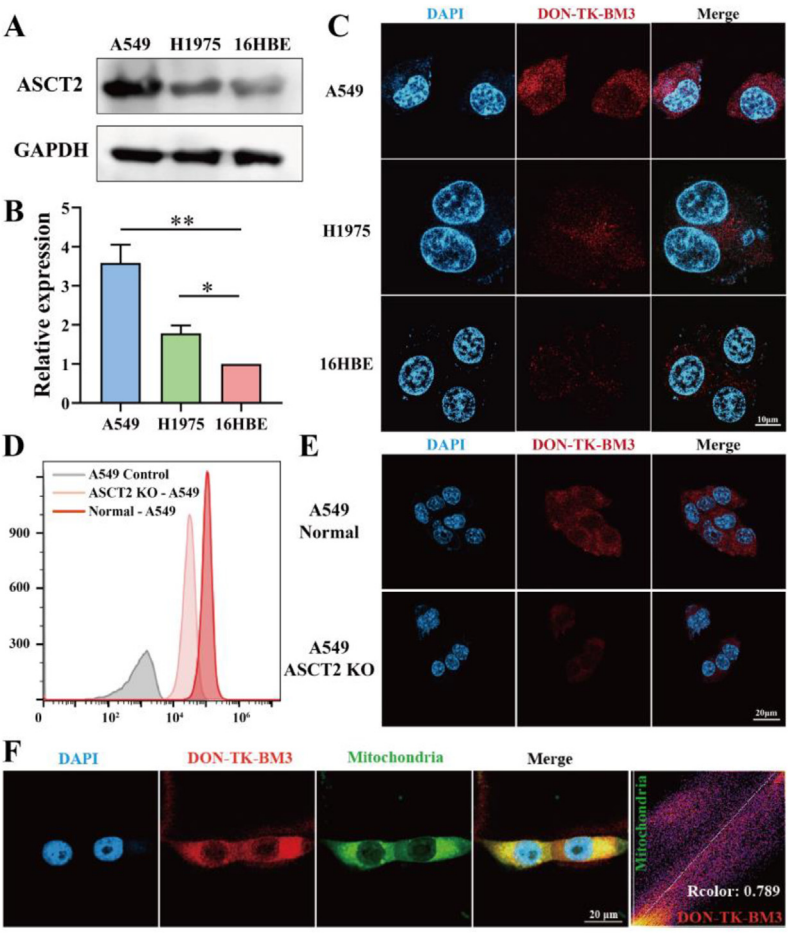

Figure 4 Cell uptake and subcellular localization of DON-TK-BM3. (A) ASCT2 protein expression levels in different types of cells assessed using Western blot analysis; (B) The gene expression of ASCT2 quantified using quantitative-PCR analysis. Data are presented as mean ± standard deviation ($n = 3$); (C) Confocal microscope images showing the uptake of DON-TK-BM3 in different cells; scale bar: 10 μm; (D−E) Flow cytometry (D) and confocal microscopy (E) images showing DON-TK-BM3 uptake in normal A549 cells and ASCT2 KO A549 cells, directly indicating the important role of ASCT2 protein in cellular uptake of DON-TK-BM3. Scale bar: 20 μm; (F) Confocal microscope images showing the colocalization of DON-TK-BM3 with mitochondria, Pearson's coefficient: 0.789; scale bar: 20 μm. Statistical analysis was performed, and significance was denoted as: $^{*}P < 0.05$, $^{**}P < 0.01$.

TK-BM3 distribution *in vivo* were shown in Supporting Information Fig. S16. The biodistribution of DON-TK-BM3 and BM3 in major organs was also evaluated (Fig. 6B). DON-TK-BM3 mainly accumulated in the tumor tissue, with faint fluorescence observed in the liver and negligible fluorescence in the heart, spleen, lungs, and kidneys. These findings demonstrate the selective homing ability of DON-TK-BM3 to tumors that possess high levels of expression of ASCT2. Overall, these results highlight the potential of DON-TK-BM3 as a promising tumor diagnostic agent. In addition, by monitoring the fluorescence signal of DK-TK-BM3 in blood vessels, it was found that the half-life of DON-TK-BM3 *in vivo* was about 31.8 min, indicating that DON-TK-BM3 had potential application *in vivo* (Supporting Information Fig. S17).

In vivo assessment of the combined effects of PDT and chemotherapy using DON-TK-BM3 was performed in A549 tumor-bearing mice models (Fig. 6C a. PBS + hv; b. DON (3 μmol/kg) + hv; c. DON-TK-BM3 (3 μmol/kg) + hv; d. DON-TK-BM3 (4 μmol/kg) + hv; all substances were administered i.v.). As shown in Fig. 6C−E and Supporting Information Fig. S18, compared with DON, DON-TK-BM3 associated with laser irradiation significantly suppressed tumor growth. Throughout the 21-day treatment period, no noticeable body weight loss was observed in the DON-TK-BM3-treated group, while the DON-treated group experienced severe weight reduction, indicating the effective reduction of DON toxicity through using the prodrug strategy (Fig. 6F). Furthermore, hematoxylin and eosin (H&E) staining analyses of tumor tissues and normal organs were performed after 21 days of treatment to evaluate the antitumor therapy effect and systemic toxicity of each drug (Fig. 6G). Compared to the PBS-treated group, the DON-TK-BM3-treated group exhibited significant apoptosis of tumor cells, while the DON-treated group induced limited tumor cell apoptosis. And the results of the acute toxicity study showed that the toxicity of DON-TK-BM3 was much lower than that of the DON group (Supporting Information Fig. S19), which indicated that the application of the pre-drug strategy could enhance the safety while improving the efficacy.

These results clearly demonstrate the effectiveness of the combined antitumor strategy comprising PDT and cascaded chemotherapy. Furthermore, H&E staining analysis, revealed significant destruction of intestinal villi structure after DON treatment,

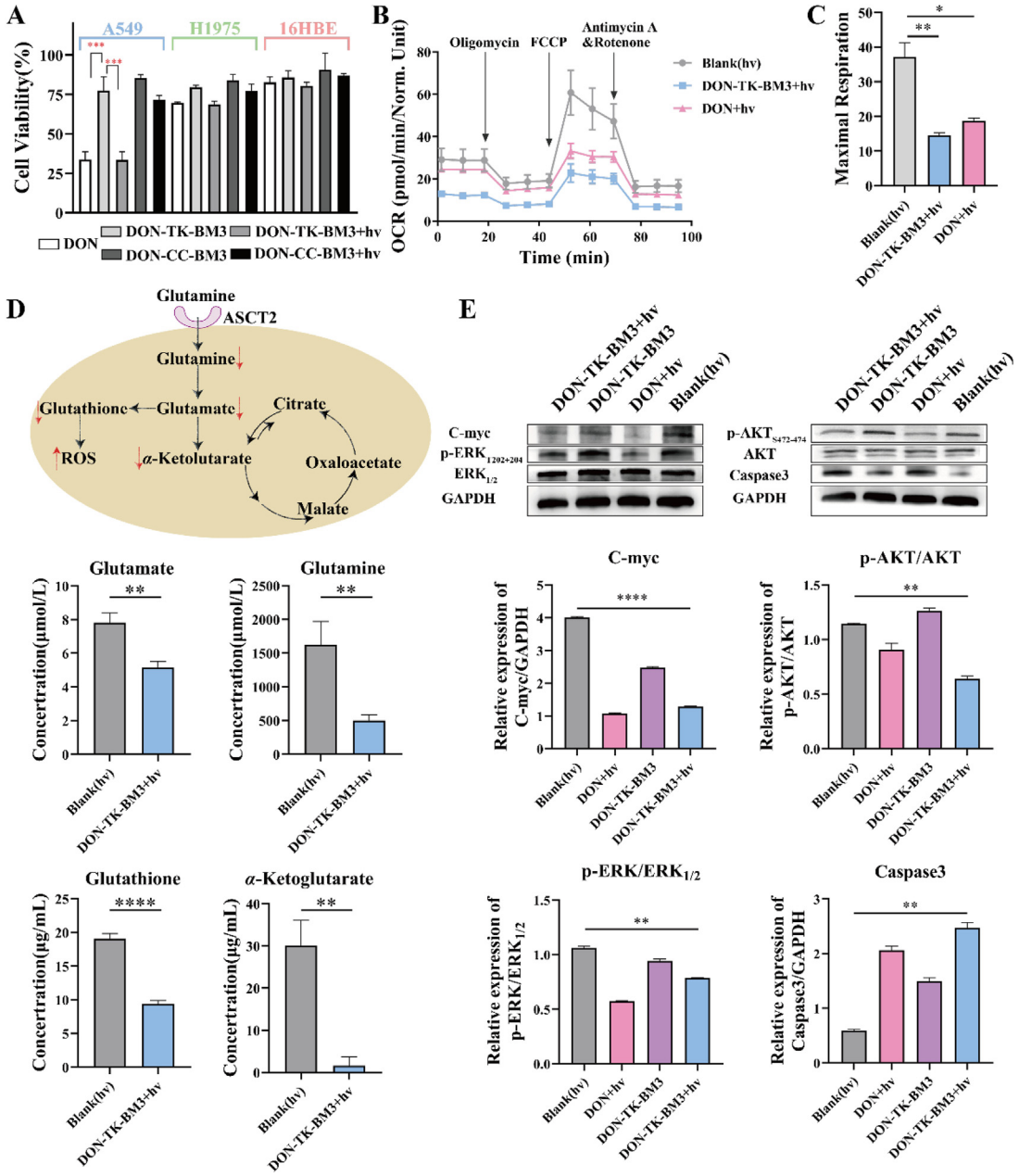

Figure 5 *In vitro* effect of DON-TK-BM3 on cell metabolism. (A) Cell viability and proliferation of A549, H1975, and 16HBE cells under different treatment conditions determined using MTT assay. Employed drug concentration was 8 μmol/L; (B) Oxygen consumption rate (OCR) assessed after different treatments using Seahorse XFe96; (C) Statistical analysis of the OCR measurements (B); (D) Effects of different treatments on amino acid metabolism; (E) The phosphorylation levels of ERK and AKT, and the level of expression of C-myc and caspase 3 determined by Western blot analysis in A549 cells. Error bars represent the standard deviation from three independent experiments. Data are presented as mean ± standard deviation. Statistical analysis was performed, and significance was denoted as: $*P < 0.05$, $**P < 0.01$, $***P < 0.001$.

while no clear intestinal damage was observed after DON-TK-BM3. This indicates that the employed prodrug strategy of DON-TK-BM3 could reduce toxicity through site-specific drug release triggered by laser. Compared to the PBS group, drug-treated mice presented no apparent abnormalities in the morphology of the heart, liver, spleen, lungs, and kidneys, as indicated by the H&E staining images of organs (Supporting Information Fig. S20). At the same time, the levels of aspartate aminotransferase (AST), alanine aminotransferase (ALT) and creatine kinase (CK) in peripheral blood of nude mice were detected to evaluate the damage of DON-TK-BM3 induced organs. Compared with the blank group of mice injected with PBS, there were no significant changes in various detection indexes in the DON-TK-BM3 treatment group (Supporting Information Fig. S21). Combined with the above experiments, we determined that DON-TK-BM3 had no effect on normal organs of mice.

To investigate the therapeutic mechanism of DON-TK-BM3, we evaluated the phosphorylation status of ERK and AKT, as well as the expression of the tumor proliferation biomarker Ki-67. This evaluation was conducted in light of the altered microenvironment

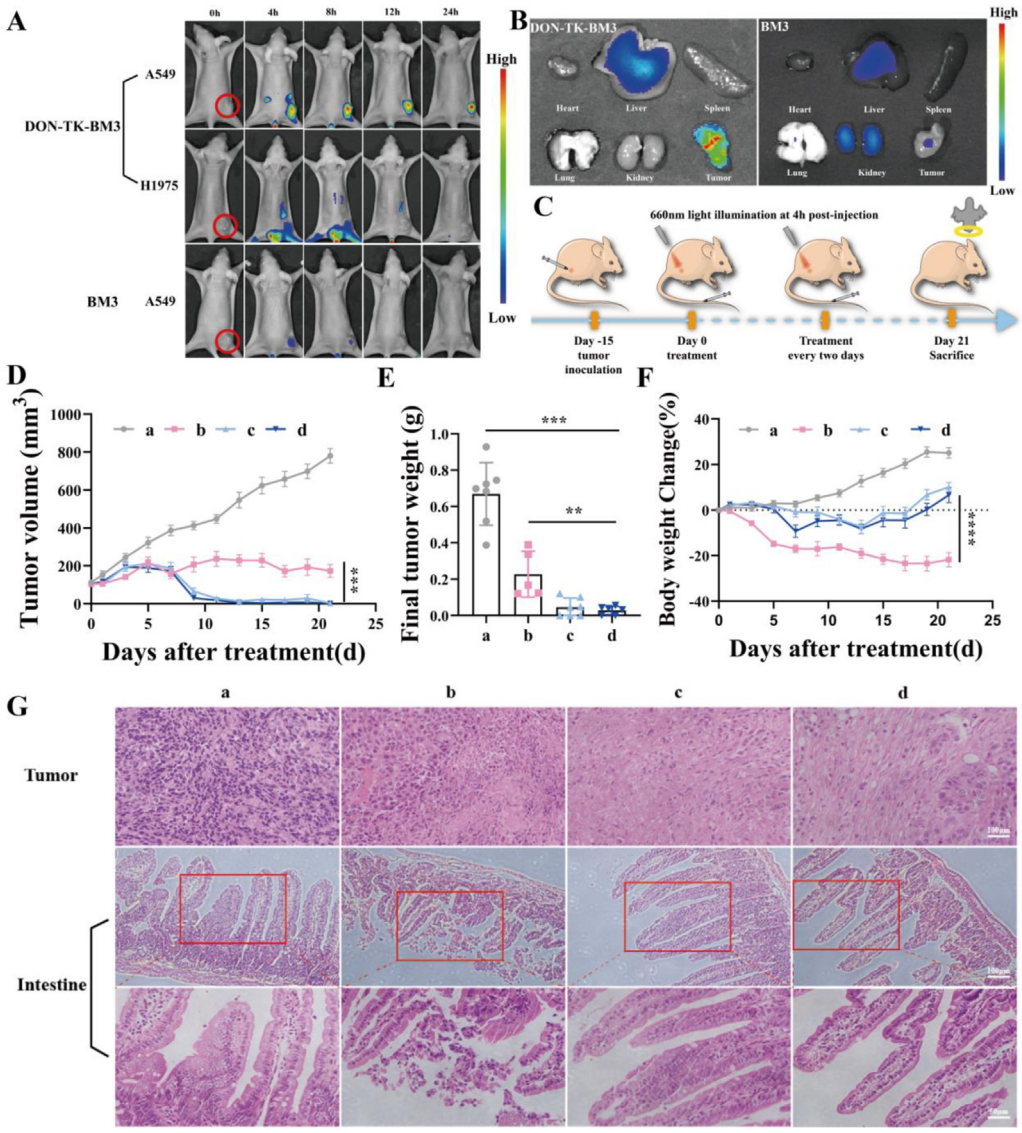

Figure 6 Biodistribution and antitumor efficacy using an A549 xenograft mouse model. (A) *In vivo* imaging of different tumor-bearing mice at various times (4, 8, 12, and 24 h) after intravenous injection of DON-TK-BM3 or BM3; (B) Fluorescence images of the internal organs 24 h after intravenous injection of DON-TK-BM3 and BM3. The color bars correspond to the detected fluorescence intensity. (C) Schematic diagram showing tumor model development and experimental protocol; (D) Tumor volume; (E) Average tumor weight; and (F) Body weight, of A549 tumor-bearing mice after different treatments ($n = 7$); (G) Hematoxylin and eosin (H&E) staining of tumor tissues (scale bar: 100 μm) and intestine (scale bar: 100 μm, and 50 μm) collected from different groups after treatment. Data were presented as mean ± standard deviation. Statistical analysis was performed, and significance was denoted as: $^{*}P < 0.05$, $^{**}P < 0.01$, $^{***}P < 0.001$, $^{****}P < 0.0001$. (a) PBS + hv; (b) DON (3 μmol/kg) + hv; (c) DON-TK-BM3 (3 μmol/kg) + hv; (d) DON-TK-BM3 (4 μmol/kg) + hv.

characterized by redox and energetic stress induced by the combination therapy. As shown in Supporting Information Fig. S22, the phosphorylation of ERK and AKT and the levels of Ki-67 were significantly suppressed by DON-TK-BM3 therapy, implying that DON-TK-BM3 disrupted tumor metabolic function, reduced energy supply to the tumor site, and inhibited tumor tissue proliferation.

2.8. Antitumor effect and immune microenvironment remodeling in LLC tumor model

Cancer cells create an anoxic, acidic, and nutrient-depleted tumor microenvironment, suppressing the tumor's immune response. DON-TK-BM3 competitively inhibited the uptake of glutamine by tumor cells, disrupting the intracellular TCA cycle and altering nutrient distribution. This has the potential to reshape the tumor immunosuppressive microenvironment. The immune activation effect of DON-TK-BM3 was investigated using LLC tumor models in C57/BL6N mice (Fig. 7A). DON-TK-BM3 showed excellent targeting properties of LLC tumor models, and under the condition of laser irradiation, DON-TK-BM3 had obvious killing effect on LLC cells (Supporting Information Fig. S23). Antitumor efficacy was evaluated for 7 days after with the tumor volume in the PBS group exceeded 1500 mm^3 (meeting the euthanasia endpoint, Fig. 7B). As shown in Fig. 7C–E, DON-TK-BM3 showed significant antitumor efficacy compared with PBS and

induced no obvious changes in the body weight of mice. Tumor tissues were isolated from mice after 7 days of treatment to investigate the immune response in the tumor site. DON has been reported to promote intratumoral immune cell maturation and invasion of $CD8^+$ and $CD4^+$ T cells. Thus, we detected the expression of CD69, a marker of early lymphocyte activation, and explored the infiltration of $CD8^+$ and $CD4^+$ T cells in tumor tissues. As shown in Fig. 7F–G, the DON-TK-BM3-treated group presented a higher level of CD69 than the PBS-treated group. Furthermore, the invasion rate of $CD4^+$ T cells in tumor tissue reached 32.2% after DON-TK-BM3 treatment, approximately twice as high as that determined after PBS administration. Flow cytometry revealed that compared to PBS, DON-TK-BM3 increased the expression of the M1 macrophage marker CD86 (to 14.5%) and decreased that of the M2 macrophage marker CD206 (Fig. 7H), which was consistent with immunohistochemistry data (Fig. 7I). These results indicated metabolic inhibition combined with PDT could promote the maturation of intratumor immune cells and produce a synergistic immune response.

Furthermore, the induction of the immune response was evaluated by measuring proinflammatory cytokine levels in tumors. Both interleukin IL-12 and IL-6, along with other signals, contribute to the maturation and activation of dendritic cells, leading to their increased ability to stimulate and regulate immune responses. Additionally, tumor necrosis factor-alpha (TNF-α), and interferon-gamma (IFN-γ) are key markers of cellular immunity and play a critical role in tumor immunotherapy. As shown in Fig. 7J, the levels of cytotoxic cytokines (TNF-α, IFN-γ, IL-6, and IL-12P70) were higher in the DON-TK-BM3-treated group than in the control group, suggesting that DON-TK-BM3 treatment could

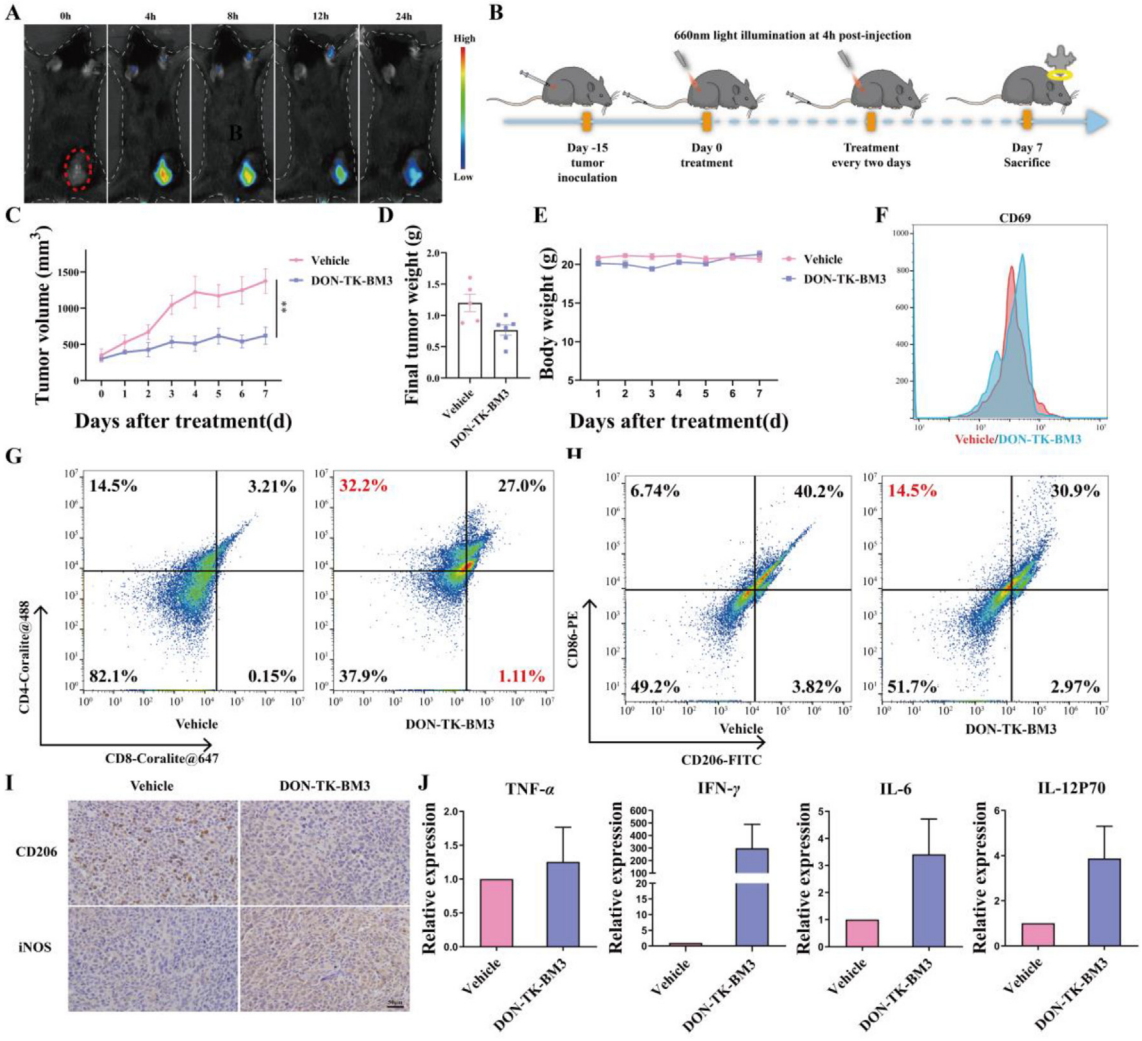

Figure 7 Antitumor efficacy and immune evaluation using an LLC tumor mouse model. (A) *In vivo* imaging at various times (4, 8, 12, and 24 h) after intravenous injection of DON-TK-BM3; (B) Schematic diagram showing tumor model development and experimental protocol; (C) Tumor volume; (D) Average tumor weight; and (E) Body weights of LLC tumor-bearing mice after different treatments ($n = 5$); (F) CD69 expression in tumor tissues assessed by flow cytometric analysis; (G) $CD4^+$ $CD8^+$ T cell ratios in tumor tissues using flow cytometric analysis; (H) Flow cytometric analysis; and (I) Immunohistochemistry images of tumor-associated macrophages (scale bar: 50 μm). CD86 and inducible nitric oxide synthase (iNOS) were used as markers of the M1 phenotype, while CD206 was used as a marker of the M2 phenotype; (J) Levels of gene expression of tumor necrosis factor-alpha (TNF-α), interferon-gamma (IFN-γ), interleukin (IL)-6, and IL-12P70 from tumor tissues assessed by quantitative-polymerase chain reaction ($n = 5$ separate samples).

promote tumor tissue necrosis. These results indicate that DON-TK-BM3 associated with PDT promotes the activation of the intratumoral immune system and potently inhibits tumor growth.

3. Conclusions

In summary, we have developed a therapeutic platform based on BM3 chromophore that allows visualization of drug release for monitoring cancer metabolic therapy *in vivo*. The drug, DON-TK-BM3, utilizes covalent thioketal bond linkers to quench its cytotoxicity. Under 660 nm irradiation, DON-TK-BM3 generates ROS, leading to the cleavage of the thioketal bond and activation of BM3 fluorescence and cytotoxicity. LC−MS analysis confirms the release of DON from DON-TK-BM3 upon laser stimulation, while confocal laser scanning microscopy shows cellular endocytosis of DON-TK-BM3 and subsequent release of BM3 fluorescence. DON-TK-BM3 exhibits excellent tumor-specific activation and immune activation potential in tumor-bearing mice. Furthermore, the prodrug displays significantly enhanced *in vivo* antitumor activity with minimal intestinal toxicity compared to free DON. Thus, our work presents a promising metabolic prodrug platform allowing the visualization of drug delivery at tumor sites and reducing the systemic toxicity of the active drug. At the same time, DON-TK-BM3 effectively promoted the activation of immune cells in tumor tissues, reversed the tumor immunosuppressive microenvironment, and laid the foundation for the challenge of tumor immunotherapy and immune restimulation. The ability of DON-TK-BM3 to allow tracking of drug release and its anticancer therapeutic efficacy in living cells and animals provides significant progress for in-depth exploration of metabolic drug application.

4. Experimental

4.1. Reagents

All reagents and solvents were commercially available at a high quality and used without further purification, unless otherwise stated. Gibco provided the FBS, DMEN medium, EDTA and PBS needed for cell culture. NMR spectra were obtained by a Bruker 300 MHz NMR spectrometer. Absorption and emission spectra were recorded on a Molecular Devices Spectra-Max ID5 Microplate Reader. Fluorescence imaging was conducted with a Leica TCS SP5 confocal scanning microscope.

4.2. General procedure for the synthesis of DON-TK-BM1−DON-TK-BM3 and DON-CC-DON、LPH-TK-BM3 (DON-TK-BM3 as example)

DON-TK-BM3 (compound **14**). Compound **11** (0.22 g, 0.39 mmol) and **7** (0.49 g, 0.58 mmol) were dissolved in DMF, and the mixture was stirred for 48 h at room temperature. Then a volume of 50 mL of ethyl ether was added and the product was separated out as a dark blue solid. The crude compound was purified by silica column chromatography using CH_2Cl_2/MeOH (8:1) as eluent to afford **14** (50 mg, 10%) as a blue solid. ^{1}H NMR (300 MHz, MeOD): δ 7.87−7.80 (m, 4H), 7.51 (d, J = 12.0 Hz, 2H), 7.41−7.27 (m, 10H), 7.13 (d, J = 9.0 Hz, 2H), 5.89 (d, J = 12.0 Hz, 2H), 5.28 (s, 4H), 5.00−4.90 (m, 1H), 4.37 (m, 1H), 3.72 (s, 6H), 2.96 (t, J = 9.0 Hz, 4H), 2.83 (t, J = 4.0 Hz, 2H), 2.62−2.33 (m, 8H), 1.71−1.67 (m, 23H), 1.34 (s, 3H), 1.24 (d, J = 6.0 Hz, 6H) ppm. ^{13}C NMR (75 MHz, MeOD): δ 172.67, 171.28, 170.97, 145.01, 140.29, 139.62, 135.04, 128.88, 127.66, 126.63, 126.17, 124.90, 119.99, 108.49, 96.60, 68.88, 55.85, 52.07, 34.90, 32.70, 29.98, 27.88, 26.17, 25.64, 25.40, 24.04, 21.02, 20.67. HRMS (ESI): m/z, calcd. for $C_{66}H_{78}N_7O_{11}S_4^-$ [M^-]: 1272.4648; found: 1272.4484.

DON-TK-BM1 (compound **12**). ^{1}H NMR (400 MHz, MeOD): Blue solid. δ 7.79 (d, J = 12.0 Hz, 2H), 7.35 (d, J = 8.0 Hz, 2H), 7.27 (t, J = 8.0 Hz, 2H), 7.12−7.07 (m, 4H), 5.97 (d, J = 12.0 Hz, 2H), 4.89−4.86 (m, 1H), 3.94 (t, J = 8.0 Hz, 4H), 3.79 (s, 4H), 3.49−3.45 (m, 8H), 2.66−2.59 (m, 8H), 2.48−2.45 (m, 4H), 1.86−1.71 (m, 8H), 1.61 (s, 11H), 1.49 (s, 8H), 1.15−1.09 (m, 6H), 0.96−0.92 (t, J = 8.0 Hz, 6H) ppm. ^{13}C NMR (75 MHz, MeOD): δ 172.65, 171.19, 170.96, 170.25, 142.76, 141.55, 140.56, 128.31, 125.44, 123.84, 121.92, 109.95, 97.37, 68.87, 55.89, 52.05, 44.69, 43.33, 35.01, 32.80, 30.04, 27.94, 26.23, 25.65, 24.76, 21.62, 20.71, 20.18, 10.45. HRMS (ESI): m/z, calcd. for $C_{58}H_{80}N_7O_5S_2^+$ [M^+]: 1018.5657; found: 1018.5658.

DON-TK-BM2 (compound **13**). ^{1}H NMR (400 MHz, MeOD): Blue solid. δ 7.77 (d, J = 16.0, 1H), 7.74 (d, J = 12.0 Hz, 1H), 7.35−7.18 (m, 4H), 7.14−6.96 (m, 4H), 6.03−5.97 (t, J = 12.0 Hz, 1H), 5.80−5.76 (t, J = 16 Hz, 1H), 4.89−4.84 (m, 1H), 4.00−3.98 (d, J = 8 Hz, 2H), 3.90 (s, 2H), 3.79 (s, 2H), 3.59−3.55 (d, J = 14 Hz, 2H), 3.21−3.20 (t, J = 1.5 Hz, 3H), 2.79−2.75 (m, 6H), 2.49−2.42 (m, 4H), 1.82 (s, 11H), 1.70−1.68 (m, 14H), 1.53 (m, 8H), 1.23−1.09 (m, 6H) ppm. ^{13}C NMR (75 MHz, MeOD): δ 171.28, 170.05, 143.09, 142.63, 141.90, 140.55, 128.34, 128.10, 125.75, 123.78, 122.61, 121.85, 121.67, 109.93, 97.42, 68.90, 55.85, 50.56, 46.22, 42.97, 29.98, 28.29, 27.86, 25.67, 25.42, 24.72, 24.41, 22.29, 21.60, 20.67. HRMS (ESI): m/z, calcd. for $C_{60}H_{82}N_7O_{11}S_4^-$ [M^-]: 1204.3161; found: 1204.3105.

DON-CC-BM3 (compound **17**). ^{1}H NMR (300 MHz, MeOD): Blue solid. δ 7.74−7.66 (m, 4H), 7.39 (d, J = 12.0 Hz, 2H), 7.25−7.13 (m, 10H), 6.99 (d, J = 9.0 Hz, 2H), 5.74 (s, 2H), 5.14 (s, 4H), 4.89−4.85 (m, 1H), 4.23−4.19 (m, 1H), 3.55 (s, 6H), 2.38−2.00 (m, 12H), 1.79 (m, 2H), 1.57 (s, 20H), 1.32−1.11 (m, 12H) ppm. HRMS (ESI): m/z, calcd. for $C_{66}H_{78}N_7O_{11}S_2^-$ [M^-]: 1208.4206; found: 1208.4679.

LPH-TK-BM3 (compound **21**).^{1}H NMR (400 MHz, MeOD): Blue solid. δ 7.85−7.78 (t, J = 12.0, 5H), 7.39−7.30 (m, 7H), 7.21 (d, J = 6.0 Hz, 10H), 7.10 (d, J = 6.0 Hz, 2H), 7.14−6.96 (m, 4H), 5.89 (s, 2H), 4.93 (s, 1H), 4.59−4.53 (t, J = 6.0 Hz, 1H), 3.68 (s, 8H), 3.22 (s, 2H), 2.99−2.92 (m, 4H), 2.87−2.79 (m, 4H), 2.51 (d, J = 9.0 Hz, 2H), 2.33 (s, 4H), 1.64 (d, J = 12.0 Hz, 18H), 1.19 (d, J = 6.0 Hz, 9H) ppm. HRMS (ESI): m/z, calcd. for $C_{70}H_{83}N_5O_{10}S_4^-$ [M^-]: 1266.4794; found ESI-MS: m/z 1266.4778.

4.3. Drug release study

Extracellular drug release: DON-TK-BM3 and DON-CC-BM3 were dissolved in pure water to a final concentration of 100 μmol/L and irradiated under 660 nm near-infrared light for 5 min, and the peak position and molecular weight were determined by LC−MS.

Intracellular drug release: A549 cells were seeded at a density of 1.5 × 10^5 cells per 20 mm glass confocal dish one day before the tests. In DMEM medium without FBS, the cells were exposed to 10 μmol/L of DON-TK-BM3 or DON-CC-BM3 for 4 h. After fixation with paraformaldehyde, laser irradiation was carried out through the transparent hole for 5 min (Fig. 3E), and fluorescence microscope was used to observe.

4.4. Cell culture

At 37 °C in a 5% CO_2 humidified incubator, A549 cells were cultivated in high-glucose DMEM, whereas H1975 and 16HBE cells were cultured in RPMI-1640 with 10% FBS and 1% penicillin–streptomycin.

4.5. The cellular uptake of DON-TK-BM3

A549 cells, H1975 cells, and 16HBE cells were planted at a density of 1.5×10^5 cells each in 12-well plates. The cells were treated with 10 μmol/L of DON-TK-BM3 solution (made in DMEM or RPMI-1640 medium) for 4 h at 37 °C after being twice rinsed in PBS. After incubation, the cells were trypsinized, washed twice with PBS, and then resuspended in 400 μL PBS. The red DON-TK-BM3 fluorescence was then seen in several cells using flow cytometry (BD Bioscience, USA). For each sample, about 3×10^4 cells were counted. Data were examined using the FlowJo program.

In order to compare the difference of DON-TK-BM3 uptake by different cells more intuitively, confocal laser fluorescence microscopy was also used in this experiment, DON-TK-BM3 fluorescence was analyzed with AF660 filter set, and Images were processed using ZEN imaging software.

Furthermore, A549 cells silencing ASCT2 protein expression by siRNA were used to investigate the effect of ASCT2 on DON-TK-BM3 transport (siRNA-F: GCCUUGGCAAGUACAUUCUTT; siRNA-R: AGAAUGUACUUGCCAAGGCTT). And V-9302, the competitive inhibitor of the ASCT2 receptor, was used so as to verify the targeting of DON prodrug group.

4.6. DON-TK-BM3 suborganelle co-localization

The localization of DON-TK-BM3 inside A549 cell was determined by confocal laser fluorescence microscopy. Colocalization tests were carried out for this purpose utilizing organelle-staining dyes. One day before the tests, A549 cells were plated on a 20 mm glass confocal dish at a density of 1.5×10^5 cells. In DMEM medium, 10 μmol/L of DON-TK-BM3 was applied to the cells for 4 h. During the final 30 min of incubation, mitochondrial green fluorescent probe (200 nmol/L) and DAPI (500 nmol/L) dyes were added. After removing the medium, the cells were thoroughly washed in PBS (4 mL) before being imaged under a microscope. Fluorescent images were observed with CLSM (LSM800, Zeiss, Germany). DON-TK-BM3 fluorescence was analyzed with AF660 filter set, Mitochondrial green fluorescent probe was analyzed with SYI00 filter set. Images were processed using ZEN imaging software.

4.7. In vitro cytotoxicity assay

In order to explore the cytotoxicity of the different compounds, phototoxicity and dark toxicity of samples (BM3, DON, DON-CC-BM3, DON-TK-BM3) were investigated. One day before the experiment, 96-well plates (7×10^3 cells per well) were seeded with A549 cells, H1975 cells, and 16HBE cells. Each well was filled with 100 μL of DMEM or RPMI-1640 having a set concentration of the BM3, DON, DON-CC-BM3, and DON-TK-BM3. The cells were then cultured for 48 h at 37 °C to test for dark toxicity. To test for phototoxicity, the cells were cultured for 12 h at 37 °C before being exposed to a laser beam (660 nm, 280 mW/cm^2) for 5 min each well. For the purpose of analyzing cell activity, MTT solution was then added.

4.8. Seahorse bioscience XFe extracellular flux analysis

Cellular OCR was measured using XF96 Extracellular Flux Analyzer. Briefly, A549 cells were seeded in Seahorse 24-well mini-plates (1.6×10^4 cells per well) and attached overnight at 37 °C with 5% CO_2. The XF96 sensor cartridge was hydrated with 200 μL of calibration buffer per well overnight at 37 °C. Cells were preincubated with DON, DON-TK-BM3 for 12 h and exposed to 660 nm laser for 10 min per well before the bioenergetic profile and the bioenergetic profiles of different cells was determined.

4.9. Western blot analysis

Light served as the experiment's backdrop setting. A549 cells were treated with a laser (660 nm, 280 mW/cm^2) for 10 min after being cultured with different samples (DON and DON-TK-BM3) for 12 h in 6-well plates. Cells were then incubated again for 24 h. Following that, NP40 lysis buffer with a PMSF protease inhibitor cocktail was used to lyse the cells in each group. An improved BCA protein assay kit was used to determine the amount of protein in the supernatant after centrifuging the cell lysate at 13,000×g for 10 min at 4 °C. The protein levels of $ERK_{1/2}$, p-$ERKT_{202+204}$, AKT, p-$AKT_{S472\text{-}474}$, C-myc, and caspase 3 were measured, and GAPDH was used as a protein loading control.

4.10. Amino acid determination

The contents of glutamine, glutamic acid, glutathione and α-ketoglutaric acid were measured. After A549 cells were treated with different samples, the contents of glutamine and glutamic acid (Glutamine/Glutamate-GloTM, Promega, USA) were measured in the supernatant of the culture medium, glutathione (GSH and GSSG Assay Kit, Beyotime, China) and α-ketoglutaric acid (α-KG ELISA Kit, Shuhua Biology, China) were measured in the cell lysate.

4.11. In vivo optical imaging, and tissue distribution

A549 tumor model was chosen in this experiment, and H1975 tumor model was used as the control group. All tumor models were subcutaneous. For *in vivo* optical imaging, each mouse was intravenously injected with 150 μL of DON-TK-BM3 and compound 7 solution (2.5×10^{-4} mol/L). At the time 0.5, 1, 2, 4, 8, 12, and 24 h after injection, mice were imaged *via* the Optical imaging system for living small animals (IVIS Lumina III, Perkin Elmer, USA) using the excitation wavelength of 660 nm. Mice were dissected 24 h following intravenous administration. Tumor, heart, liver, spleen, lung, and kidneys from mice were collected for the investigation on tissue distribution of DON-TK-BM3.

4.12. Antitumor study in A549 tumor model

The guidelines for the care and use of laboratory animals were followed when caring for the animals. Female nude mice that were six to seven weeks old were kept in conventional cages with free access to food and water and were kept in an isolator for small animals under aseptic conditions. Before being used in

experiments, all animals spent at least 7 days becoming used to the facilities.

To investigate the pharmacokinetic characteristics of DON-TK-BM3 in mice, preexposure of the jugular vein was performed in mice, and DON-TK-BM3 was injected into the tail vein at a dose of 3 μmol/kg. After injection, a laser probe was used to monitor the fluorescence of the jugular vein, and the fluorescence signal intensity was recorded every 0.5 min.

BALB/c-nu mice bearing 100−200 mm^3 A549 tumor were randomly divided into four groups ($n = 7$). All groups were i.v. injected with PBS, DON (3 μmol/kg), DON-TK-BM3 (3 μmol/kg), DON-TK-BM3 (4 μmol/kg) every two days. Tumors in each group were exposed to laser irradiation (660 nm, 280 mW/cm^2, 15 min) at 4 h after samples injection. Tumor size (calculated as $\pi \times$ length $\times$ $width^2/2$) and body weight were monitored every day. On Day 21, all mice were sacrificed, H&E staining and blood biochemical analysis (aspartate aminotransferase (AST), alanine aminotransferase (ALT) and creatine kinase (CK)) were performed to analyze tissue damage after various treatments. In addition, Ki-67 staining was carried out to verify cancer cell proliferation, p-AKT and p-ERK staining were warried out to verify drugs induced apoptosis of cancer cell.

4.13. *Antitumor effect and immune responses in LLC tumor model*

C57/BL6N mice bearing 400−500 mm^3 LLC tumors were randomly divided into two groups ($n = 7$). All groups were i.v. injected with PBS and DON-TK-BM3 (4 μmol/kg) every two days. Tumor in each group were exposed to laser irradiation (660 nm, 280 mW/cm^2, 20 min) at 4 h after samples injection. Tumor size and body weight were measured everyday. Mice were sacrificed 7 days after the initial injection. At the end of the experiment, tumors were excised, part of each tumor was paraffin embedded for CD206 and iNOS staining, while the other part was immediately frozen in −80 °C for subsequent analysis. To examine immune responses after treatment, $CD8^+/CD4^+$, CD69 T cells and $CD86^+/CD206^+$ Macrophages infiltrated in tumor tissue were analyzed using flow cytometry. The expression of IFN-γ, IL-6, IL-12P70, TNF-α, and other inflammatory factors in tumor tissues was examined by PCR as well.

4.14. *Molecular docking analysis of DON-TK-BM3 with the ASCT2 protein*

The human ASCT2 structure (PDB ID 7BCQ) was prepared using the MOE2022.02, and the active site was defined by the cocrystal ligand, through Site Finder. Then, DON was docked using the general modes, and the pharmacophoric conformation of DON was considered the reference for DON-TK-BM3 to generate conformations within the ASCT2 pocket. Finally, the DON-TK-BM3 complex was used for molecular dynamics simulations (Desmond program, 20 ns) and binding free energy calculations (MM-GBSA).

4.15. *In vitro metabolic stability experiment*

All compounds were tested for *in vitro* plasma stability in human plasma, with DON-TK-BM1 dissolved in dimethyl sulfoxide (DMSO), DON-TK-BM2 and DON-TK-BM3 dissolved in pure water, and then diluted to a final concentration of 100 μmol/L in a 100 μL human plasma system. The samples were incubated at 37 °C for 0, 10, 30, 60, 120 min, and carried out in triplicate. The reaction was terminated by adding 300 μL of cold acetonitrile. The sample was centrifuged, and drug metabolism was monitored by HPLC.

4.16. *In vivo toxicity experiments*

C57BL/6J mice were randomly divided into 4 groups, including Vehicle, DON (30 μmol/kg), DON-TK-BM3 (30 μmol/kg) and DON-TK-BM3 (40 μmol/kg) group, with 5 mice in each group. The compounds were prepared into suspension (saline: DMSO = 98:2; *v/v*), daily tail vein injection for 7 consecutive days. The survival status and weight changes of mice were observed and recorded.

Acknowledgments

We acknowledge financial support from the National Natural Science Foundation of China (82072058, 91859204, 82073702), Natural Science Foundation of Jiangsu Province for Excellent Young Scientists (Grant BK20211580, China), and Qinglan Project of Jiangsu Province of China. “Double First-Class” university project (CPUQNJC22 05, China).

Author contributions

Wen Li, Jiali Huang and Chen Shen contributed equally to this work. Yi Ma and Jin-Lei Bian conceived the project. Wen Li, Jiali Huang, Chen Shen, Weiye Jiang, Xi Yang, and Jingxuan Huang performed the experiment and analyzed the results. Yueqing Gu and Zhiyu Li provided useful suggestions to this work. Wen Li, Chen Shen and Jiali Huang wrote the manuscript.

Conflicts of interest

The authors declare no conflicts of interest.

Appendix A. Supporting information

Supporting data to this article can be found online at https://doi.org/10.1016/j.apsb.2023.10.020.

References

1. Reinfeld BI, Madden MZ, Wolf MM, Chytil A, Bader JE, Patterson AR, et al. Cell-programmed nutrient partitioning in the tumor microenvironment. *Nature* 2021;**593**:282−8.
2. Zachary ES, Zachary TS, Joseph MS, Chi VD. Targeting cancer metabolism in the era of precision oncology. *Nat Rev Drug Discov* 2022;**21**:14162.
3. Vander Heiden MG, Cantley LC, Thompson CB. Understanding the Warburg effect: the metabolic requirements of cell proliferation. *Science* 2009;**324**:1029−33.
4. Shi J, Ju R, Gao H, Huang Y, Guo L, Zhang D. Targeting glutamine utilization to block metabolic adaptation of tumor cells under the stress of carboxyamidotriazole-induced nutrients unavailability. *Acta Pharm Sin B* 2022;**12**:759−73.
5. Du D, Liu C, Qin M, Zhang X, Xi T, Yuan S, et al. Metabolic dysregulation and emerging therapeutical targets for hepatocellular carcinoma. *Acta Pharm Sin B* 2022;**12**:558−80.

6. Ward PS, Patel J, Wise DR, Abdel-Wahab O, Bennett BD, Coller HA, et al. The common feature of leukemia-associated IDH1 and IDH2 mutations is a neomorphic enzyme activity converting alpha-ketoglutarate to 2-hydroxyglutarate. *Cancer Cell* 2010;**17**:225−34.
7. Stine ZE, Schug ZT, Salvino JM, Dang CV. Targeting cancer metabolism in the era of precision oncology. *Nat Rev Drug Discov* 2022;**21**:141−62.
8. Lemberg KM, Vornov JJ, Rais R, Slusher BS. We're not "DON" yet: optimal dosing and prodrug delivery of 6-diazo-5-oxo-L-norleucine. *Mol Cancer Therapeut* 2018;**17**:1824−32.
9. Rais R, Jančařík A, Tenora L, Nedelcovych M, Alt J, Englert J, et al. Discovery of 6-diazo-5-oxo-l-norleucine (DON) prodrugs with enhanced CSF delivery in monkeys: a potential treatment for glioblastoma. *J Med Chem* 2016;**59**:8621−33.
10. Earhart RH, Amato DJ, Chang AY, Borden EC, Shiraki M, Dowd ME, et al. Phase II trial of 6-diazo-5-oxo-L-norleucine versus aclacinomycin-A in advanced sarcomas and mesotheliomas. *Invest N Drugs* 1990;**8**:113−9.
11. Magill GB, Myers WP, Reilly HC, Putnam RC, Magill JW, Sykes MP, et al. Pharmacological and initial therapeutic observations on 6-diazo-5-oxo-1-norleucine (DON) in human neoplastic disease. *Cancer* 1957;**10**:1138−50.
12. Rahman A, Smith FP, Luc PT, Woolley PV. Phase I study and clinical pharmacology of 6-diazo-5-oxo-L-norleucine (DON). *Invest N Drugs* 1985;**3**:369−74.
13. Tenora L, Alt J, Dash RP, Gadiano AJ, Novotná K, Veeravalli V, et al. Tumor-targeted delivery of 6-diazo-5-oxo-l-norleucine (DON) using substituted acetylated lysine orodrugs. *J Med Chem* 2019;**62**:3524−38.
14. Nedelcovych MT, Tenora L, Kim BH, Kelschenbach J, Chao W, Hadas E, et al. *N*-(Pivaloyloxy)alkoxy-carbonyl prodrugs of the glutamine antagonist 6-diazo-5-oxo-l-norleucine (DON) as a potential treatment for HIV associated neurocognitive disorders. *J Med Chem* 2017;**60**:7186−98.
15. Klán P, Šolomek T, Bochet CG, Blanc A, Givens R, Rubina M, et al. Photoremovable protecting groups in chemistry and biology: reaction mechanisms and efficacy. *Chem Rev* 2013;**113**:119−91.
16. Janeková H, Russo M, Ziegler U, Štacko P. Photouncaging of carboxylic acids from cyanine dyes with near-infrared light. *Angew Chem Int Ed Engl* 2022;**61**:e202204391.
17. Šolomek T, Wirz J, Klán P. Searching for improved photoreleasing abilities of organic molecules. *Acc Chem Res* 2015;**48**:3064−72.
18. Zhang Y, Yan C, Zheng Q, Jia Q, Wang Z, Shi P, et al. Harnessing hypoxia-dependent cyanine photocages for *in vivo* precision drug release. *Angew Chem Int Ed Engl* 2021;**60**:9553−61.
19. Zhang J, Chai X, He XP, Kim HJ, Yoon J, Tian H. Fluorogenic probes for disease-relevant enzymes. *Chem Soc Rev* 2019;**48**:683−722.
20. Li JC, Luo Y, Pu KY. Electromagnetic nanomedicines for combinational cancer immunotherapy. *Angew Chem Int Ed Engl* 2021;**60**:12682−705.